This article has been accepted for publication in a future issue of this journal, but has not been fully edited. Content may change prior to final publication. Citation information: DOI 10.1109/ACCESS.2019.2918926, IEEE Access

IEEE Access
Multidisciplinary ⋮ Rapid Review ⋮ Open Access Journal

# Deep Generative Adversarial Networks for Thin-section Infant MR Image Reconstruction

**Jiaqi Gu[1], Zeju Li[2], Yuanyuan Wang[3], Senior Member, IEEE, Haowei Yang[4], Zhongwei Qiao[5], and Jinhua Yu[6*], Member, IEEE**

[1,2]The School of Information Science and Technology, Fudan University, Shanghai, 200433 China
[4,5]The Children's Hospital of Fudan University, Shanghai, China
[3,6]The Department of Electronic Engineering, Fudan University, Shanghai, China, also with the Institute of Functional and Molecular Medical Imaging, Fudan University, Shanghai, China, and also with the Key Laboratory of Medical Imaging Computing and Computer Assisted Intervention of Shanghai, China

Corresponding author: Jinhua Yu (e-mail: jhyu@fudan.edu.cn), Zhongwei Qiao (e-mail: zqiao@fudan.edu.cn).

This work was supported by the National Natural Science Foundation of China (61471125) and the National Basic Research Program of China (2015CB755500).

**ABSTRACT** Due to their high spatial resolution, thin-section magnetic resonance (MR) images serve as ideal medical images for brain structure investigation and brain surgery navigation. However, compared with the clinically widely used thick-section MR images, thin-section MR images are less available due to the imaging cost. Thin-section MR images of infants are even scarcer but are quite valuable for the study of human brain development. Therefore, we propose a method for the reconstruction of thin-section MR images from thick-section images. A two-stage reconstruction framework based on generative adversarial networks (GANs) and a convolutional neural network (CNN) is proposed to reconstruct thin-section MR images from thick-section images in the axial and sagittal planes. A 3D-Y-Net-GAN is first proposed to fuse MR images from the axial and sagittal planes and to achieve the first-stage thin-section reconstruction. A 3D-DenseU-Net followed by a stack of enhanced residual blocks is then proposed to provide further detail recalibrations and structural corrections in the sagittal plane. In this method, a comprehensive loss function is also proposed to help the networks capture more structural details. The reconstruction performance of the proposed method is compared with bicubic interpolation, sparse representation, and 3D-SRU-Net. Cross-validation based on 35 cases and independent testing based on two datasets with totally 114 cases reveal that, compared with the other three methods, the proposed method provides an average 23.5% improvement in peak signal-to-noise ratio (PSNR), 90.5% improvement in structural similarity (SSIM), and 21.5% improvement in normalized mutual information (NMI). Quantitative evaluation and visual inspection demonstrate that our proposed method outperforms those methods by reconstructing more realistic results with better structural details.

**INDEX TERMS** Deep learning, infant magnetic resonance (MR) images, super-resolution reconstruction, thick-section, thin-section.

## I. INTRODUCTION

Thin-section head magnetic resonance (MR) images typically have a slice thickness of 1 mm and a spacing gap of zero. The high spatial resolution of thin-section head MR images is ideal for brain structure analysis, volumetric measurement, and surgery navigation. Thin-section head MR images, however, are not always available. Clinically routine head MR images are typically thick-section images with a slice thickness of 4 mm to 6 mm and a spacing gap of 0.4 mm to 1 mm. The higher section thickness leads to a lower spatial resolution, which limits the usage of thick-section MR images in brain-related research.

Compared with imaging data for adults, brain MR images of infants are even more valuable because these images provide great insight into human brain development after birth. The acquisition of infant brain MR images, however, is even more difficult since MR imaging, let alone thin-section imaging, is rarely performed on infants without sufficient reasons. This situation inspired us to develop a method that can provide a spatial resolution comparable to thin-section MR images by using available thick-section images. A thin-section MR image reconstruction method is thus proposed in this paper.

This reconstruction method can also be used to normalize the image layer spacing. In a multi-center, multi-device scenario, proposed method can be used to normalize MR images obtained at different layer spacings to a uniform layer spacing, which is very beneficial for data-driven researches,



2169-3536 (c) 2019 IEEE. Translations and content mining are permitted for academic research only. Personal use is also permitted, but republication/redistribution requires IEEE permission. See http://www.ieee.org/publications_standards/publications/rights/index.html for more information.

This article has been accepted for publication in a future issue of this journal, but has not been fully edited. Content may change prior to final publication. Citation information: DOI 10.1109/ACCESS.2019.2918926, IEEE Access



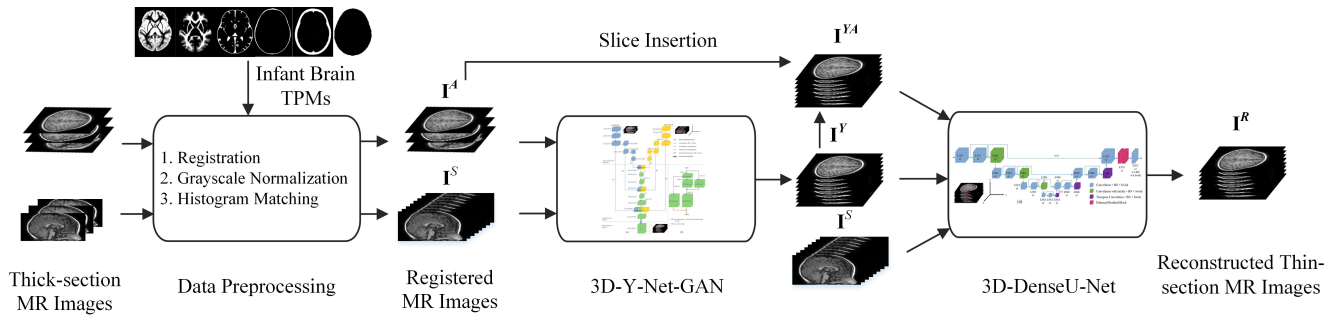


**FIGURE 1. The proposed two-stage framework for thin-section MR image reconstruction. The first stage is 3D-Y-Net-GAN, and the second stage is 3D-DenseU-Net. TPMs represent tissue probability maps, which will be discussed in later sections.**

such as human brain development statistics based on image big data.

Thin-section MR image reconstruction was considered a multiplanar MR image registration problem. For example, Mahmoudzadeh *et al.* [1] applied traditional interpolation algorithms to thick-section MR images in all three planes and combined them with the iterative registration algorithm optimized automatic image registration (OAIR) [2] with the guidance of a pixelwise loss function. The reconstruction results of this algorithm are visually improved but focus only on adult head MR images with limited consideration of structural similarity (SSIM) among human brains. Moreover, thin-section MR image reconstruction can be handled as a frame interpolation task. As proposed in [3], a decomposition-reconstruction method based on the rules of organ consistency is adopted to obtain a higher inter-slice resolution. Thin-section image reconstruction can also be considered a super-resolution problem. Yang *et al.* [4] proposed a trainable method to reconstruct high-resolution images by utilizing the same sparse representation between low-resolution image patches and their high-resolution counterparts. With the development of deep learning (DL) techniques, convolutional neural networks (CNN) and generative adversarial networks (GANs) have gained momentum recently, especially in the image super-resolution field. Accordingly, thin-section MR image reconstruction, if considered as a nonisotropic super-resolution problem, will benefit a great deal from the powerful modeling capacity of deep neural networks. For example, Heinrich *et al.* [5] recently applied a 3D-SRU-Net for isotropic super-resolution from nonisotropic three-dimensional (3-D) electron microscopy. Our group [6] proposed a residual-network-based 3D-SRGAN to reconstruct adult thin-section MR images from thick-section MR images, however only the reconstruction in the axial plane was considered. In addition, CNNs and GANs have been widely utilized to improve the resolution of MR images [7], [8]. Compared to traditional algorithms, DL algorithms show superior potential in thin-section MR image reconstruction by not only increasing reconstruction performance but also reducing the reconstruction time to seconds.

In this paper, the task is to combine the multiplanar feature fusion and 3-D nonisotropic super-resolution problems. Our proposed framework is inspired by several state-of-the-art DL architectures. First, U-Net [9], as it performs well in the biomedical segmentation field, distinguishes itself in feature fusion problems through multiscale convolution and upscaling. Super-resolution generative adversarial neural networks (SRGANs) [10] are empirically proven to have remarkable performance in the super-resolution field, as they extract both low- and high-frequency information from images. In addition, enhanced deep residual networks (EDSR) [11], a new residual architecture that won first prize in the NTIRE 2017, provide an efficient approach to recovering high-resolution images. Inspired by the above state-of-the-art models, we propose a two-stage reconstruction framework to apply the mapping from thick-section MR images in the axial and sagittal planes to their axial thin-section counterparts. Specifically, the first stage is a least-squares GAN (LSGAN) [12] with a newly proposed 3D-Y-Net generator, which is designed to fuse axial and sagittal thick-section MR images and map them onto the thin-section image space. The second stage is a cascade connection of 3D-DenseU-Net and enhanced residual blocks, designed to increase statistical metrics and eliminate artifacts via further detail refinement. A 3-D gradient correction loss and a self-adaptive Charbonnier loss are proposed to concentrate the generator's optimization attention and capture high-frequency differential information. We then evaluate the performance of the proposed two-stage framework by comparing the reconstruction results with the ground truth, showing that our proposed method is more effective than three representative methods, comprising bicubic interpolation [13], sparse representation [4], and 3D-SRU-Net [5]. We also undertake two experiments to further validate the contribution of multiplanar image fusion and our proposed comprehensive loss function. Finally, the conclusion summarizes the paper.

## II. PROPOSED METHOD

### A. OVERVIEW

CNNs have outperformed many traditional algorithms in the image super-resolution field. Via hierarchical spatial convolution and optional nonlinearity, CNNs can learn the prior knowledge from low-level and high-level features extracted from images and accordingly recover super-resolved images through upsampling operations such as fractionally-strided convolution [14] and sub-pixel convolution [15]. Recently, with an increasing number of state-of-the-art CNN models, e.g., EDSR, SRCNN [16], and



2169-3536 (c) 2019 IEEE. Translations and content mining are permitted for academic research only. Personal use is also permitted, but republication/redistribution requires IEEE permission. See http://www.ieee.org/publications_standards/publications/rights/index.html for more information.

This article has been accepted for publication in a future issue of this journal, but has not been fully edited. Content may change prior to final publication. Citation information: DOI 10.1109/ACCESS.2019.2918926, IEEE Access



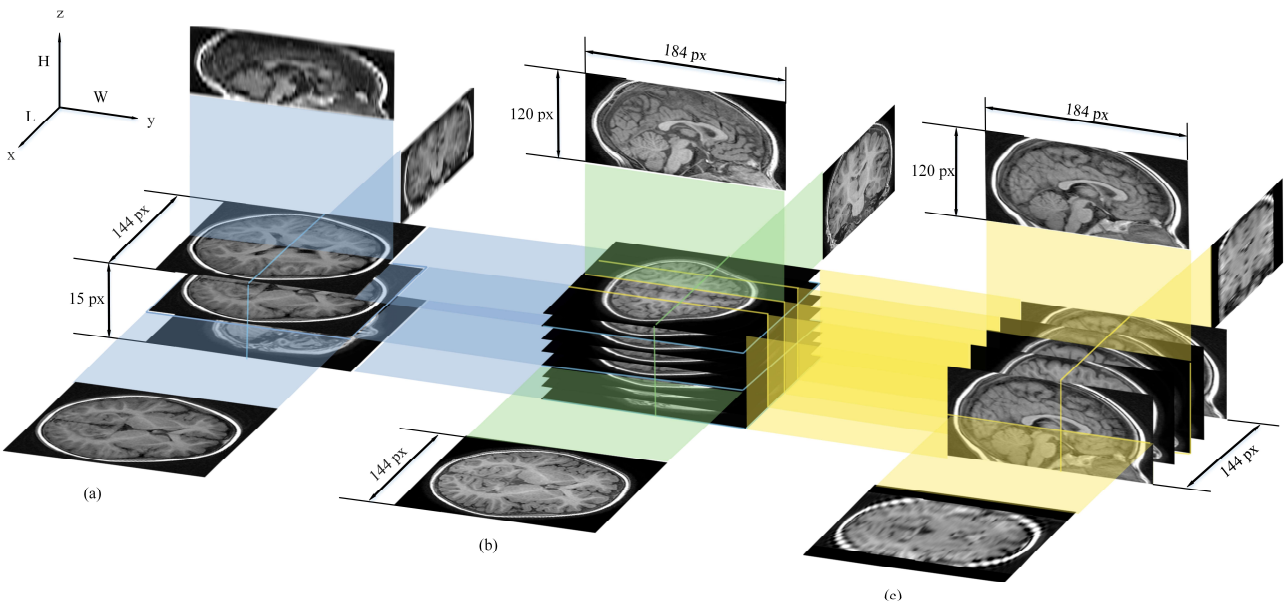


**FIGURE 2.** **(a) 15 slices of normalized axial thick-section MR images, (b) 120 slices of normalized axial thin-section MR images, (c) 120 slices of normalized sagittal thick-section MR images. *x*, *y*, and *z* represent three axes in the coordinate system we use to describe the volumes. *L*, *W*, and *H* represent image sizes of MR images along *x*, *y*, and *z* axes, respectively. The yellow and blue lines illustrate their relative spatial locations. *px* is short for pixel.**

VDSR [17], GANs are becoming gradually integrated with these popular CNN models in order to preserve high-frequency information. Under the supervision of the discriminator, the generator is driven to maximize the distribution similarity between the generated data and the real data, thus generating results that are more realistic. However, recently proposed super-resolution models mainly seek to upscale both dimensions of two-dimensional (2-D) images by the same factor [7], [15], [18], [19], [20], [21]. Even if several models are extended to handle 3-D images [5], [6], low-resolution images in multiple planes barely make a collaborative contribution in a single framework. In this study, we propose a two-stage reconstruction framework based on axial and sagittal thick-section MR images to reconstruct corresponding axial thin-section MR images with an upscaling factor of 8, as shown in Fig. 1. In our framework, multiplanar thick-section MR images are fully fused by our proposed 3D-Y-Net-GAN and 3D-DenseU-Net to recover thin-section images collaboratively. In the following sections, we demonstrate the details of the proposed two-stage reconstruction framework and our proposed comprehensive loss function. To better demonstrate the task, relative spatial locations of thick-section and thin-section MR images are shown in Fig. 2.

## B. NETWORK ARCHITECTURE

In this section, we introduce our proposed two-stage reconstruction framework. The first stage is a 3D-Y-Net-GAN consisting of a 3D-Y-Net generator and a conditional discriminator, which produces primary thin-section MR images for subsequent detail correction. The second stage is a 3D-DenseU-Net followed by a stack of enhanced residual blocks for final detail recalibration. The inputs are registered axial thick-section MR images, denoted as $\mathbf{I}^A$ with size $L\times W\times H$, and registered sagittal thick-section MR images, denoted as $\mathbf{I}^S$ with size $L\times W\times rH$ where $r$ represents the upscaling factor along the z-axis. The outputs are thin-section MR images, denoted as $\mathbf{I}^R$ with size $L\times W\times rH$. Note that $L$, W, and H represent spatial sizes along $x$, $y$, and $z$ axes respectively.

### 1) 3D-Y-NET-GAN

As the first stage of the whole framework, a 3D-Y-Net-GAN is proposed to take $\mathbf{I}^A$ and $\mathbf{I}^S$ as inputs and reconstruct thin-section MR images with an upscaling factor of $r$, denoted as $\mathbf{I}^Y$. The generator consists of three branches: 1) feature extraction (FE), 2) feature fusion (FF), and 3) reconstruction. The detailed network structure of the generator is illustrated in Fig. 3(a). In our case, $r$ is set to 8, and we adopt a patch-based training strategy to reduce computational cost. Specifically, at the first stage, the size of the patches for $\mathbf{I}^A$ is 32×32×15 and the size of the patches for $\mathbf{I}^S$ and $\mathbf{I}^Y$ is 32×32×120. Note that, for inference, instead of image patches, full-size MR images are used as inputs.

#### a) Feature Extraction Branches

For the axial FE branch, 3-D convolutional layers are adopted to extract features from input images, and maxpooling layers with unbalanced strides of [1,2,1] or [2,1,1] are adopted to generate differently sized feature maps at different levels. Notably, maxpooling layers can ignore certain minute structural discrepancies, such that the negative impact induced by misalignment after registration would be mitigated to some degree. To clarify, the 3-D convolutional layer is Convolution+Batch Normalization+Swish. Specifically, Swish [22] is a new activation function that overcomes the dead-neuron problems caused by ReLU. In our framework, we set the untrainable parameter in Swish to be 1. The outputs of the



2169-3536 (c) 2019 IEEE. Translations and content mining are permitted for academic research only. Personal use is also permitted, but republication/redistribution requires IEEE permission. See http://www.ieee.org/publications_standards/publications/rights/index.html for more information.

This article has been accepted for publication in a future issue of this journal, but has not been fully edited. Content may change prior to final publication. Citation information: DOI 10.1109/ACCESS.2019.2918926, IEEE Access



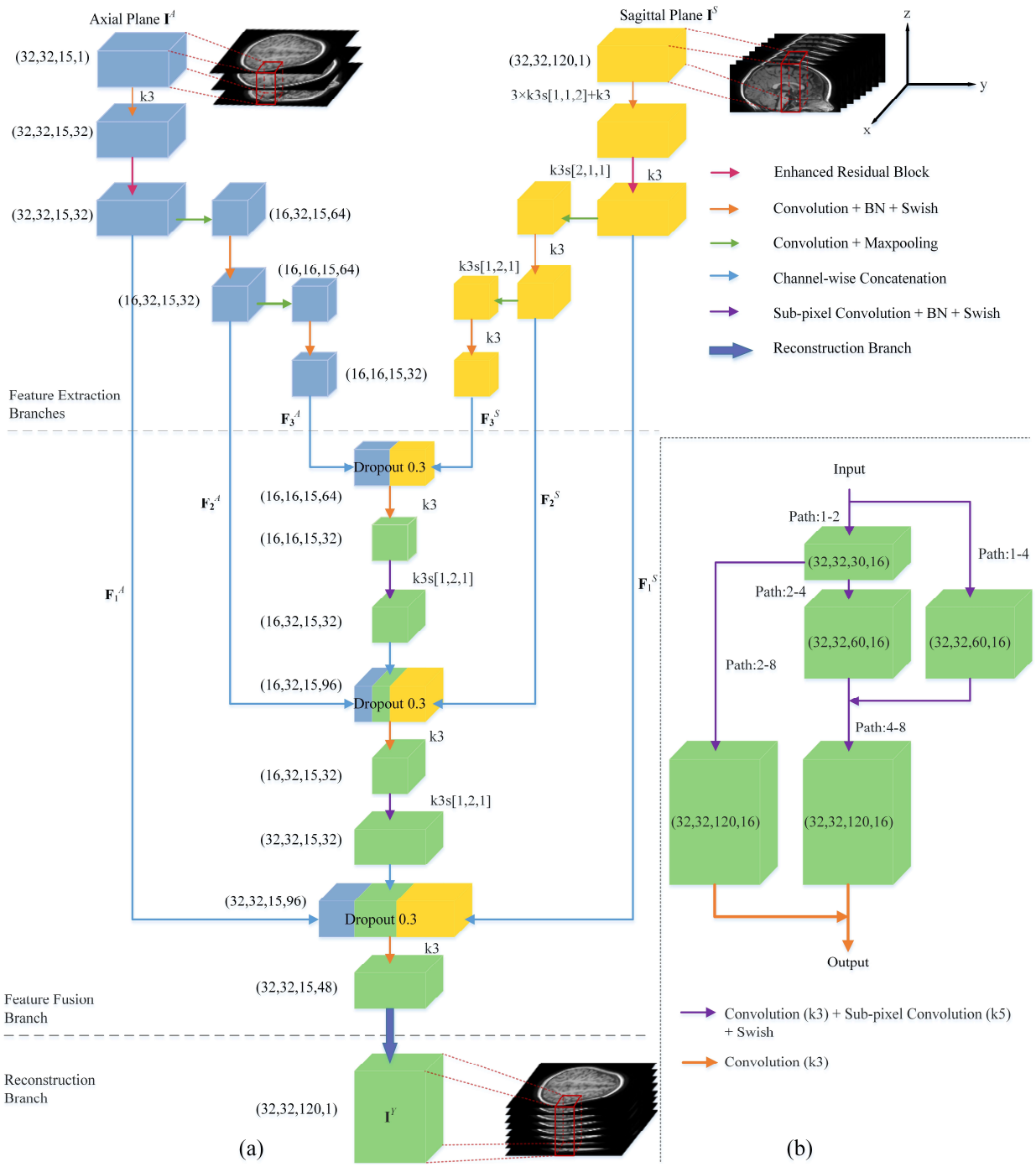


**FIGURE 3. (a) shows the network structure of 3D-Y-Net, e.g., (32,32,15,64) represents 64-channel feature maps with a spatial size of 32×32×15, e.g., k3s [1,2,1] represents a convolution kernel size of 3×3×3 with strides of [1,2,1]. Unless specified, kernel sizes, strides, and feature map shapes are identical between axial and sagittal branches, thus most parameters are only shown in either branch. *Dropout 0.3* represents the dropout operation with a drop rate of 0.3. Red frameworks represent patches for training; (b) shows the structure of the reconstruction branches. *Path* represents the upscaling process, e.g., *Path 1-4* means upsampling images with sizes of *L×W×H* to images with sizes of *L×W×4H*. The intersection of two arrows represents channel concatenation before convolution.**

axial FE branch are feature maps in three scales: $\mathbf{F}_1^A$ ($L\times W\times H$), $\mathbf{F}_2^A$ ($L\times W/2\times H$), and $\mathbf{F}_3^A$ ($L/2\times W/2\times H$). The sagittal FE branch is generally of the same structure as the axial FE branch, which generates similar outputs $\mathbf{F}_1^S$ ($L\times W\times H$), $\mathbf{F}_2^S$ ($L\times W/2\times H$), and $\mathbf{F}_3^S$ ($L/2\times W/2\times H$). However, given the size discrepancy between $\mathbf{I}^A$ and $\mathbf{I}^S$, an extra preprocessing module consisting of 3 convolutional layers with strides of [1,1,2] is appended to its entry.

### b) Feature Fusion Branches

The FF branch is a topological inversion of FE branches. At each level, the FF branch upsamples multiscale feature maps through sub-pixel convolution. Concretely, sub-pixel



2169-3536 (c) 2019 IEEE. Translations and content mining are permitted for academic research only. Personal use is also permitted, but republication/redistribution requires IEEE permission. See http://www.ieee.org/publications_standards/publications/rights/index.html for more information.

This article has been accepted for publication in a future issue of this journal, but has not been fully edited. Content may change prior to final publication. Citation information: DOI 10.1109/ACCESS.2019.2918926, IEEE Access

**FIGURE 4. Network structure of the conditional discriminator. Note that the slope of the negative part of the Leaky ReLU is set to 0.2. $\mathbf{I}^{GT}$ is the real sample, $\mathbf{I}^Y$ is the fake sample, $\mathbf{I}^A$ and $\mathbf{I}^S$ are inputs of the generator. *k* represents the kernel size, and *f* represents the number of filters. All the dropout rates are set to 0.3.**

convolution [15] is a normal convolution followed by a pixel shuffler, which is an efficient substitution for transpose convolution. The means by which FE and FF branches are connected at three levels is a design inspired by the U-Net structure, which fully fuses multiscale features, guarantees the structural alignment, and avoids the gradient-vanishing problem.

#### c) Reconstruction Branches

The detailed network structure of the reconstruction branch is shown in Fig. 3(b). This branch is specially designed for a large upscaling factor of 8. Instead of a sequential connection of 3 upsampling layers with an upscaling factor of 2, which might stretch the images and generate severe artifacts for lack of adequate information forwarding or feature reuse, we adopt a multipath upscaling strategy to mitigate such artifacts. Specifically, the outputs of *Path 2-4* and *Path 1-4* are concatenated as the inputs of *Path 4-8*; the outputs of *Path 4-8* and *Path 2-8* are concatenated as the inputs of the final convolution. We use $\mathbf{I}^Y$ to represent the output of the reconstruction branch, which is also the final output of the 3D-Y-Net generator.

#### d) Discriminator

Given that the unsupervised GAN model is adopted here to solve a supervised regression problem, the original discriminator that gives high scores to realistic samples is not theoretically applicable for this supervised regression problem because our generator does not sample prior vectors from random noise. Instead, our discriminator is designed to be of a conditional structure [23], [24]. Specifically, the discriminator can recognize the input of the generator such that it can classify a reconstruction mapping from thick-section images to thin-section images as "real" or "fake." The detailed network structure is shown in Fig. 4. This structure takes $\mathbf{I}^A$, $\mathbf{I}^S$, and $\mathbf{I}^Y$ as fake inputs and $\mathbf{I}^A$, $\mathbf{I}^S$, and $\mathbf{I}^{GT}$ (ground-truth images) as real inputs and outputs a score tensor for later computation of loss functions.

### 2) 3D-DENSEU-NET

As the second stage of the whole framework, a 3D-DenseU-Net followed by a stack of 2 enhanced residual blocks is proposed for detail recalibration, whose network structures are shown in Fig. 5. The key point of detail recalibration lies in information reuse. To reuse axial thick-section images, we simply insert $\mathbf{I}^A$ into $\mathbf{I}^Y$ according to their corresponding spatial positions, which is denoted as $\mathbf{I}^{YA}$. Through this way, axial thick-section images can be easily used to correct axial images. When reusing sagittal thick-section images, slice insertion is not applied. The main reason is that we would like to reuse all slices in $\mathbf{I}^S$. But if $\mathbf{I}^S$ and sagittal-slice-inserted $\mathbf{I}^Y$ are both used as inputs of the second stage network, more information of sagittal slices than that of axial slices will be introduced into 3D-DenseU-Net, which could decrease the image quality in the axial plane. Based on the above consideration, We set $\mathbf{I}^Y$, $\mathbf{I}^S$, and $\mathbf{I}^{YA}$ as inputs of the 3D-DenseU-Net and let $\mathbf{I}^R$ denote the final output thin-section MR images. Notably, the dense architecture we adopt allows the output of the previous convolutional layers to be passed down to several convolutional layers, which, according to [21], [25], can fully leverage low-level and high-level features. Additionally, to prevent blurriness and structural distortion caused by top-level and bottom-level skip connections, we apply value decay before channelwise concatenation to balance feature maps at different levels. Moreover, the tail enhanced residual blocks are also designed for similar consideration, since shallow features passing through the top-level skip connection could corrupt the final outputs. Without traditional batch normalization layers, enhanced residual blocks are also preferred as they cut down GPU RAM usage, thus allowing larger batch size in training phase.

Given limited GPU capacity, there is a trade-off between convergence rate and receptive field. Specifically, relatively larger patch size leads to larger receptive field, thus more useful information can be seen by convolution kernels. But it also reduces the maximum batch size we could use, which could harm the convergence rate especially when batch size is already small. After hyperparameter search, we train 3D-DenseU-Net based on randomly sampled patches with size of 48×48×48 to strike a balance between convergence and receptive field.

It is worth noting that 3D-DenseU-Net and 3D-Y-Net-GAN are trained separately instead of end-to-end. Two major reasons can account for this. First, separate training



2169-3536 (c) 2019 IEEE. Translations and content mining are permitted for academic research only. Personal use is also permitted, but republication/redistribution requires IEEE permission. See http://www.ieee.org/publications_standards/publications/rights/index.html for more information.

This article has been accepted for publication in a future issue of this journal, but has not been fully edited. Content may change prior to final publication. Citation information: DOI 10.1109/ACCESS.2019.2918926, IEEE Access



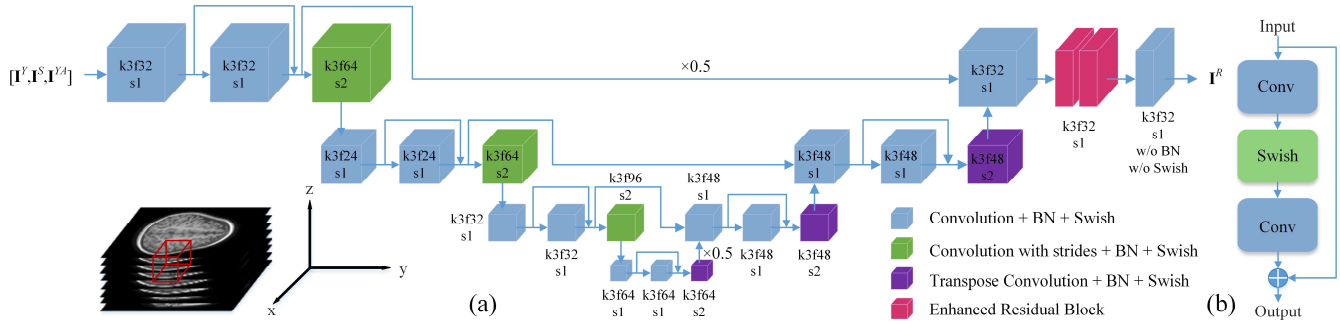


**FIGURE 5. Network structure of the second stage. (a) is 3D-DenseU-Net; (b) is the enhanced residual block. Red framework represents patches for training. ×*0.5* represents value decay by a factor of 0.5.**

could guarantee the functionality of initial reconstruction as designed for 3D-Y-Net-GAN, and also decouple the functionality of two stages. Second, end-to-end training of two 3-D DL models are currently not feasible on our GPU resources if using acceptable batch size.

### 3) LOSS FUNCTION

To train the 3D-Y-Net-GAN to learn the mapping from $\boldsymbol{I}^A$ and $\mathbf{I}^S$ to $\mathbf{I}^Y$, we need to search the set of network parameters $\boldsymbol{\theta}_G$ and obtain the optimal parameters $\hat{\boldsymbol{\theta}}_G$ that minimize the generator's loss function $L_G$, which is described as in (1), where $G$ is taken as the generator and $\mathbf{I}^{GT}$ is taken as the ground truth.

$$\hat{\boldsymbol{\theta}}_G = \arg\min_{\boldsymbol{\theta}_G} \mathrm{L}_G\left(\mathrm{G}\left(\mathbf{I}^A, \mathbf{I}^S\right), \mathbf{I}^{GT}\right) \tag{1}$$

To find a loss function that evaluates the difference between the generated images and the ground-truth images, we design a loss function that consists of a self-adaptive Charbonnier loss, a 3-D gradient correction loss, an adversarial loss, and an $\ell_2$ weight regularization term:

$$\mathrm{L}_G = \mathrm{L}_{SC}^G + \lambda_1 \mathrm{L}_{GC}^G + \lambda_2 \mathrm{L}_{AD}^G + \lambda_3 \mathrm{L}_{WR}^G \tag{2}$$

where $\lambda_1$, $\lambda_2$, and $\lambda_3$ represent the respective terms' weights. The above four components will be further discussed in the following paragraphs. Given the second stage 3D-DenseU-Net is not based on adversarial learning, we train it with the same loss function $\mathrm{L}_G$ as used for 3D-Y-Net-GAN except that $\lambda_2$ is set to 0.

#### a) Self-adaptive Charbonnier Loss

In supervised regression problems, the $\ell_1$ and $\ell_2$ norms are widely used because pixelwise restriction is practically important to guarantee the basic SSIM. However, the $\ell_2$ norm often leads to overly smooth results, and the $\ell_1$ norm penalizes the deviation of the prediction from the ground truth indiscriminately. In one study [20], a Charbonnier loss, a differentiable variant of the $\ell_1$ norm, showed better performance and higher robustness than an $\ell_1$ and $\ell_2$ norm. In another study [5], a cubic-weighted mean square error (MSE) loss was introduced to emphasize the performance in "difficult" areas, which represent areas with relatively large pixelwise differences between generated images and ground truth. However, the difference between the ground truth and upsampled images through bicubic interpolation will not always be a good indicator of the actual difficult areas along the training process and is even worse when facing a large upscaling factor. Therefore, we propose the use of the dynamic coefficients calculated by the difference between the current generated images and the ground truth to weigh the robust Charbonnier loss:

$$\mathrm{L}_{SC}^G = \frac{1}{rLWH} \sum_{x,y,z=1,1,1}^{L,W,rH} \sqrt{\left(\mathbf{I}_{x,y,z}^{GT} - \mathbf{I}_{x,y,z}^{Y}\right)^2 + \varepsilon} \cdot \left(\frac{1}{2} + \frac{\left(\mathbf{I}_{x,y,z}^{GT} - \mathbf{I}_{x,y,z}^{Y}\right)^2}{2\max\left(\left(\mathbf{I}^{GT} - \mathbf{I}^{Y}\right)^2\right)}\right) \tag{3}$$

where $\varepsilon$ is a small value, which is set to $10^{-6}$, $(\cdot)^2$ performs element-wise square if input is a tensor, and $\max(\cdot)$ function calculates the global maximum element of a tensor, which outputs a scalar value.

#### b) 3-D Gradient Correction Loss

A Charbonnier loss merely addresses the pixelwise difference, which may lead to inadequate attention to the second-order differential information. This being the case, we adopt a 3-D gradient correction loss to explicitly exert a second-order constraint between adjacent pixels along the $x$, $y$, and z-axes, which can help our model generate sharper edges:

$$\begin{aligned} L_{GC}^G = {} & \mathbb{E}\left[\left(\nabla_x \mathbf{I}_{x,y,z}^{GT} - \nabla_x \mathbf{I}_{x,y,z}^{Y}\right)^2\right] \\ & + \mathbb{E}\left[\left(\nabla_y \mathbf{I}_{x,y,z}^{GT} - \nabla_y \mathbf{I}_{x,y,z}^{Y}\right)^2\right] \\ & + \mathbb{E}\left[\left(\nabla_z \mathbf{I}_{x,y,z}^{GT} - \nabla_z \mathbf{I}_{x,y,z}^{Y}\right)^2\right] \end{aligned} \tag{4}$$

#### c) Adversarial Loss

To make the generated images more realistic, we utilize a conditional discriminator to supervise the learning process of the generator. Taking into account robustness and implementation efficiency, we use the LSGAN loss as the adversarial loss. For the conditional discriminator, its loss function is defined as follows:

$$\mathrm{L}^D = \frac{1}{2}\mathbb{E}\left[\left(\mathrm{D}\left(\mathbf{I}^{GT}, \mathbf{I}^A, \mathbf{I}^S\right) - 1\right)^2 + \left(\mathrm{D}\left(\mathbf{I}^Y, \mathbf{I}^A, \mathbf{I}^S\right) - 0\right)^2\right] \tag{5}$$



2169-3536 (c) 2019 IEEE. Translations and content mining are permitted for academic research only. Personal use is also permitted, but republication/redistribution requires IEEE permission. See http://www.ieee.org/publications_standards/publications/rights/index.html for more information.

This article has been accepted for publication in a future issue of this journal, but has not been fully edited. Content may change prior to final publication. Citation information: DOI 10.1109/ACCESS.2019.2918926, IEEE Access



where $D$ represents the discriminator and $\mathbb{E}$ represents the mathematical expectation, which practically calculates the mean value of the output tensor. To make it clear, the discriminator tries to make the score of ground truth close to 1 and that of fake inputs close to 0.

The generator tries to fool the conditional discriminator by increasing the score of the fake samples. Accordingly, the adversarial loss for the generator is shown below:

$$\mathrm{L}_{AD}^{G} = \mathbb{E}\left[\left(\mathrm{D}\left(\mathbf{I}^{Y},\mathbf{I}^{A},\mathbf{I}^{S}\right)-1\right)^{2}\right] \tag{6}$$

Notably, the balance between the generator and the discriminator is crucial when training GANs, which means we need to strike a balance between the adversarial loss and the Charbonnier loss. Therefore, we consider this adversarial loss an auxiliary term in the generator's loss function and set a small value for its weight $\lambda_2$. The hyperparameter setting of $\lambda_1$, $\lambda_2$, and $\lambda_3$ will be further discussed in the Experimental Results section.

#### d) $\ell_2$ Weight Regularization Loss

Theoretically, parameters with smaller norms lead to lower model complexity, which is indicative of a decreased likelihood of encountering the overfitting problem. Thus, we adopt an $\ell_2$ weight regularization loss to mitigate overfitting problem in this study:

$$\mathrm{L}_{WR}^{G} = \sum \left\|\mathbf{W}_{G}\right\|_{2}^{2} \tag{7}$$

where $\mathbf{W}_G$ represents all the kernel weights of the generator, and $\|\cdot\|_2$ represents the $\ell_2$ norm.

## III. EXPERIMENTAL RESULTS

To demonstrate the effectiveness of multiplanar MR image fusion, we conduct an ablation experiment among 3 cases: 1) our full framework with axial and sagittal images as inputs (Ours Full), 2) a partial version of our method with only axial images as input (Ours Partial Axial), and 3) a partial version of our method with only sagittal images as input (Ours Partial Sagittal). Specifically, for Ours Partial Axial and Ours Partial Sagittal, we modify the 3D-Y-Net generator to have two FE or FF branches and discard the input $\mathbf{I}^{S}$ or $\mathbf{I}^{YA}$, respectively, at the second stage. After the above network modifications, we have two partial versions of our proposed framework, which only leverage thick-section MR images in a single plane.

To validate our proposed comprehensive loss function, we conduct another ablation experiment among four cases: 1) $\ell_1$ norm+$\mathrm{L}_{GC}$+$\mathrm{L}_{AD}$+$\mathrm{L}_{WR}$, 2) $\mathrm{L}_{SC}$+$\mathrm{L}_{GC}$+$\mathrm{L}_{WR}$, 3) $\mathrm{L}_{SC}$+$\mathrm{L}_{AD}$+$\mathrm{L}_{WR}$, and 4) $\mathrm{L}_{SC}$+$\mathrm{L}_{GC}$+$\mathrm{L}_{AD}$+$\mathrm{L}_{WR}$.

To evaluate our proposed reconstruction method, three representative methods and our proposed first-stage network are used for comparison: 1) traditional bicubic interpolation [13], 2) sparse representation (SR) [4], 3) 3D-SRU-Net [5], and our proposed first stage 3D-Y-Net-GAN. Each of those comparison methods will be detailed below.

Traditional bicubic interpolation [13] is an untrainable algorithm that predicts a certain pixel with adjacent 16 pixels. SR [4] is a trainable method that seeks a SR for each patch of the low-resolution image and then uses the coefficients of this representation to generate its high-resolution counterpart. Specifically, we train the coupled dictionaries based on the 2-D slices in the sagittal plane. As described in the introduction, 3D-SRU-Net has been proposed for isotropic super-resolution reconstruction from nonisotropic 3-D electron microscopy. In [5], low-resolution and high-resolution images are jointly leveraged when training this variant of the original U-Net to predict high-resolution images from their blurred counterparts. In our paper, we increase the depth of its network and append 3 convolutional layers with strides of [2,1,1] to its entry, similar to that in our second-stage framework, such that its upscaling factor is extended to 8 and can take the same inputs as our proposed first-stage networks. We also show the reconstruction results of our proposed first stage network 3D-Y-Net-GAN in order to validate the effectiveness of the second stage network.

For quantitative evaluation, we adopt metrics, including peak signal-to-noise ratio (PSNR), SSIM, and normalized mutual information (NMI), for image quality assessment. Note that we clip the pixels that are out of the valid dynamic range [-1,1] and cast the generated MR images and the ground truth to an 8-bit grayscale. PSNR is defined as follows:

$$PSNR = 20\cdot\log_{10}\left(\frac{MAX_{I}}{\sqrt{\frac{1}{rLWH}\sum_{x,y,z}\left(\mathbf{I}_{x,y,z}^{R}-\mathbf{I}_{x,y,z}^{GT}\right)^{2}}}\right) \tag{8}$$

where $MAX_I$ represents the maximum pixel value, which is 255 in this case; and $r$ represents the upscaling factor, which is 8 in this case. $L$, $W$, and $H$ represent the spatial size of the generated MR images, which are 144, 184, and 120, respectively, in this case. SSIM measures the structural similarity between two images by calculating their cross-correlation, which is defined as follows:

$$SSIM = \frac{(2\mu_a\mu_b + c_1)(2\sigma_{ab} + c_2)}{(\mu_a^{\ 2} + \mu_b^{\ 2} + c_1)(\sigma_a^{\ 2} + \sigma_b^{\ 2} + c_2)} \tag{9}$$

where $\mu_a$ and $\mu_b$ represent the respective mean values of two images; $\sigma_a^2$ and $\sigma_b^2$ represent the respective variances; $\sigma_{ab}$ represents the covariance of the two images; and $c_1=(k_1L)^2$, $c_2=(k_2L)^2$ are two constants that prevent the dominator from being 0, where $k_1$ and $k_2$ are typically set to be 0.01 and 0.03, respectively; and $L$ represents the dynamic range of the pixel values, which is set to be 255 in our case. NMI measures the mutual dependence between two variables, which is defined as follows:

$$\begin{cases} H(X) = -\sum_{x_i\in X} p(x_i)\log p(x_i) \\ H(X,Y) = -\sum_{y_j\in Y}\sum_{x_i\in X} p(x_i,y_j)\log p(x_i,y_j) \\ NMI(X,Y) = 2\dfrac{H(X)+H(Y)-H(X,Y)}{H(X)+H(Y)} \end{cases} \tag{10}$$



2169-3536 (c) 2019 IEEE. Translations and content mining are permitted for academic research only. Personal use is also permitted, but republication/redistribution requires IEEE permission. See http://www.ieee.org/publications_standards/publications/rights/index.html for more information.

This article has been accepted for publication in a future issue of this journal, but has not been fully edited. Content may change prior to final publication. Citation information: DOI 10.1109/ACCESS.2019.2918926, IEEE Access



TABLE I
IMAGING PARAMETERS OF OUR DATASET.

| Imaging Parameters | Axial Thin-section Images | Axial Thick-section Images | Sagittal Thick-section Images |
|---|---|---|---|
| Imaging Pulse Sequence | 3D T1 BRAVO | T1 FLAIR | T1 FLAIR |
| Voxel Size (mm) | 0.5×0.5×1 | 0.4687×0.4687×6.5 | 6.5×0.4687×0.4687 |
| Number of Slices | 126-153 | 19 | 19 |
| Repetition Time (ms) | 8.17 | 1450 | 2291.30 |
| Echo Time (ms) | 3.17 | 25.10 | 25.30 |
| Inversion Time (ms) | 450 | 627.84 | 749.77 |
| Flip Angle (degree) | 12 | 111 | 111 |

where *H(X)* is the entropy of variable *X*, *H(X,Y)* is the joint entropy of *X* and *Y*, $p(x_i)$ is the marginal probability distribution function of $x_i$, and $p(x_i, y_i)$ is the joint probability distribution function of $x_i$ and $y_i$. Higher PSNR, SSIM, and NMI mean that the generated MR images are much closer to the ground truth.

### A. DATA AND PREPROCESSING

We validate our two-stage framework on the reconstruction of thin-section infant head MR images. Thick-section and thin-section MR images of 154 infants aged 2 to 5 years old were collected from the Children's Hospital of Fudan University, Shanghai, China. For each individual infant, we collected axial thick-section, sagittal thick-section, and axial thin-section MR images with the specific imaging parameters listed in Table I. We randomly selected 40 samples for the cross-validation dataset, another 65 samples as the independent testing dataset 1, and the rest 49 samples as the independent testing dataset 2. Note that the collection time interval of two independent testing sets is half a year. We applied spatial normalization, grayscale normalization, and histogram matching to our raw MR image data for data preprocessing. We use preprocessed thick-section images as inputs of our model, and preprocessed thin-section images as the ground truth during the training phase.

Given different imaging parameters (e.g. field of view) and various intensities between thin-section and thick-section MR images, we observed spatial misalignment and intensity imbalance in raw image-domain MRI data, for which raw MR images in DICOM format can not be directly used in our experiments. Thus we preprocess all raw MR images as followings. For registration, we apply unified spatial normalization to all the MR images using MATLAB tools SPM12 [26], to mitigate spatial misalignment between thin-section and thick-section MR images. We firstly transform MR images from Digital Imaging and Communications in Medicine (DICOM) format to Neuroimaging Informatics Technology Initiative (NIfTI) format. Secondly, we segment the infant brain atlas [27] to generate the full version of tissue probability maps (TPMs) which contain probability maps of various tissues in the image data, including gray matter (GM), white matter (WM), cerebrospinal fluid (CSF), skull, scalp, and air mask. Thirdly, SPM12 estimates nonlinear deformation field that best aligns the generated TPMs to the individual's MR images. Then, MR images are warped according to their own estimated deformation field. Finally, we obtain $\mathbf{I}^A$ of size 144×184×15, $\mathbf{I}^S$ and $\mathbf{I}^{GT}$ of size 144×184×120. For detailed configuration of registration, we set voxel size of thin-section images to 1×1×1 mm$^3$, axial thick-section images to 1×1×8 mm$^3$, and sagittal thick-section images to 1×1×1 mm$^3$. Besides, we use ICBM Asian brain template in affine regularization and adopt appropriate bounding box such that registered MR images have the exact spatial size as illustrated in Fig. 2. Other configurations are kept default. After registration, possible misalignment due to various spatial positions and head shapes is minimized. Note that the field of view of sagittal thick-section MR images is smaller than that of thin-section images, thus there are uncovered head areas at each side in $\mathbf{I}^S$, as shown in Fig. 2(c). To avoid the structural incompleteness of $\mathbf{I}^S$, we upsample corresponding areas in $\mathbf{I}^A$, and simply use them to fill the uncovered areas in $\mathbf{I}^S$. Since SPM12 can not guarantee successful registration on all samples, we actually found 5 poorly-registered samples in the cross-validation dataset, which were accordingly excluded from it. Thus, 35 samples comprise the actual cross-validation dataset for all experiments.

Also, given that registered MR images have a 16-bit grayscale with various intensities among different subjects, we normalize intensities of all MR images into [-1,1], using simple linear transformation. Then, we apply a histogram-matching algorithm to all MR images with a fixed sample as reference to eliminate histogram imbalance.

In order to enlarge our training dataset and mitigate the overfitting problem for the data-driven DL model, we adopt data augmentation by applying radial transformation [28] and mirror reflection to our training dataset.

### B. EXPERIMENTAL SETTINGS

We adopt 5-fold cross-validation on the cross-validation dataset to evaluate our framework. For fold *s*, we divide the cross-validation dataset of 35 samples randomly into 2 parts, with 7 samples as the validation data and the other 28 as the training data. For data augmentation, we apply radial transformation and mirror reflection to the training data, such that it is enlarged to 336 samples at the first stage and 56 samples at the second stage. All of the validation procedures are applied to 5 iterations. To further validate the generalization of our proposed model, we select a certain model with the best performance in the cross-validation and evaluate it on independent testing dataset 1 of 65 samples,



2169-3536 (c) 2019 IEEE. Translations and content mining are permitted for academic research only. Personal use is also permitted, but republication/redistribution requires IEEE permission. See http://www.ieee.org/publications_standards/publications/rights/index.html for more information.

This article has been accepted for publication in a future issue of this journal, but has not been fully edited. Content may change prior to final publication. Citation information: DOI 10.1109/ACCESS.2019.2918926, IEEE Access



TABLE II
QUANTITATIVE EVALUATION OF THIN-SECTION MR IMAGE RECONSTRUCTION METHODS USING DIFFERENT INPUT DATA: PSNR, SSIM, AND NMI

| Dataset | Input plane(s) | PSNR (dB) | | SSIM | | NMI | |
|---|---|---|---|---|---|---|---|
| | | Mean (std.) | Med. | Mean (std.) | Med. | Mean(std.) | Med. |
| Cross-validation Dataset | Axial Only | 19.53(0.79) | 19.60 | 0.63(0.04) | 0.64 | 0.20(0.01) | 0.20 |
| | Sagittal Only | 19.65(0.99) | 19.57 | 0.67(0.05) | 0.69 | **0.21(0.02)** | **0.21** |
| | Axial and Sagittal | **19.75(0.85)** | **19.69** | **0.69(0.05)** | **0.71** | **0.21(0.02)** | **0.21** |
| Independent Testing Dataset | Axial Only | 18.77(0.96) | 18.84 | 0.62(0.05) | 0.63 | 0.19(0.01) | 0.19 |
| | Sagittal Only | 19.06(0.75) | 19.03 | 0.64(0.03) | 0.65 | 0.19(0.01) | 0.20 |
| | Axial and Sagittal | **19.12(0.85)** | **18.98** | **0.66(0.03)** | **0.66** | **0.20(0.01)** | **0.20** |

Bold text indicates the best performance.

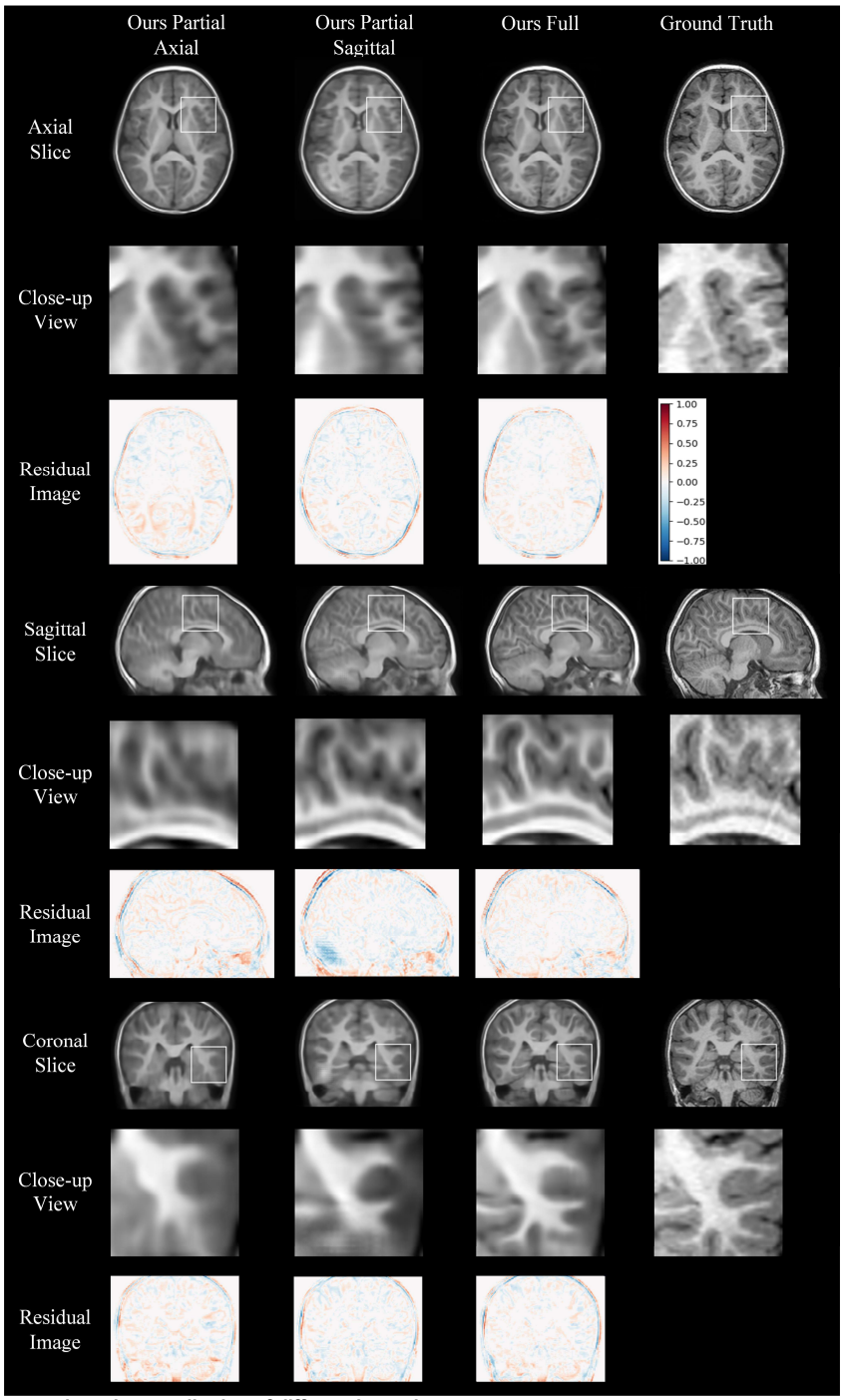


**FIGURE 6.** **Visual comparison to show the contribution of different input data.**



2169-3536 (c) 2019 IEEE. Translations and content mining are permitted for academic research only. Personal use is also permitted, but republication/redistribution requires IEEE permission. See http://www.ieee.org/publications_standards/publications/rights/index.html for more information.

This article has been accepted for publication in a future issue of this journal, but has not been fully edited. Content may change prior to final publication. Citation information: DOI 10.1109/ACCESS.2019.2918926, IEEE Access



TABLE III
QUANTITATIVE EVALUATION OF THIN-SECTION MR IMAGE RECONSTRUCTION METHODS USING DIFFERENT LOSS FUNCTIONS: PSNR, SSIM, AND NMI

| $\ell_1$ norm | $L_{SC}$ | $L_{GC}$ | $L_{AD}$ | PSNR (dB) | | SSIM | | NMI | |
|---|---|---|---|---|---|---|---|---|---|
| | | | | Mean (std.) | Med. | Mean (std.) | Med. | Mean(std.) | Med. |
| × | | × | × | 19.96(0.57) | 20.09 | 0.70(0.03) | 0.71 | 0.21(0.01) | 0.21 |
| | × | × | | 19.92(0.63) | 19.75 | 0.70(0.03) | 0.71 | 0.21(0.01) | 0.21 |
| | × | | × | 19.94(0.56) | 20.03 | 0.70(0.03) | 0.71 | 0.21(0.01) | 0.21 |
| | × | × | × | **20.03(0.61)** | **20.06** | **0.70(0.03)** | **0.71** | **0.21(0.01)** | **0.21** |

× represents involvement of the corresponding term in the loss function. Bold text indicates the best performance.

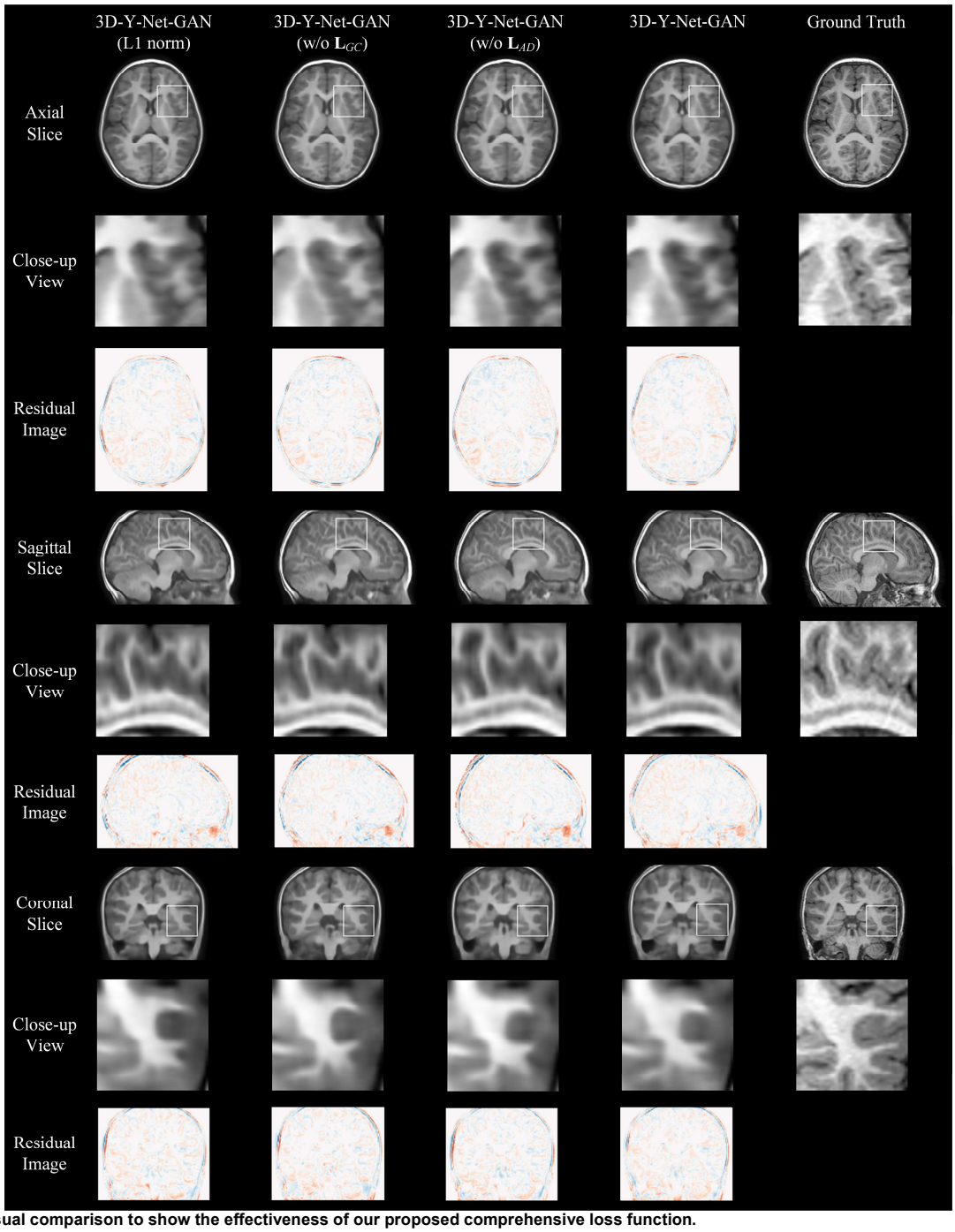


**FIGURE 7.** **Visual comparison to show the effectiveness of our proposed comprehensive loss function.**

and independent testing dataset 2 of 49 samples, whose collection time interval is half a year.

For 3D-Y-Net-GAN, we randomly sample 12 patches per volume with a size of 32×32×15 for $\mathbf{I}^A$ and 32×32×120 for



2169-3536 (c) 2019 IEEE. Translations and content mining are permitted for academic research only. Personal use is also permitted, but republication/redistribution requires IEEE permission. See http://www.ieee.org/publications_standards/publications/rights/index.html for more information.

This article has been accepted for publication in a future issue of this journal, but has not been fully edited. Content may change prior to final publication. Citation information: DOI 10.1109/ACCESS.2019.2918926, IEEE Access



TABLE IV
QUANTITATIVE EVALUATION OF THIN-SECTION MR IMAGE RECONSTRUCTION METHODS: PSNR, SSIM, NMI, AND MAE

| Dataset | Methods | Input plane(s) | PSNR (dB) | | SSIM | | NMI | | MAE | |
|---|---|---|---|---|---|---|---|---|---|---|
| | | | Mean (std.) | Med. | Mean (std.) | Med. | Mean(std.) | Med. | Mean(std.) | Med. |
| Cross-validation Dataset | Bicubic [13] | Axial Only | 14.59(0.44) | 14.58 | 0.31(0.04) | 0.30 | 0.17(0.01) | 0.17 | 32.96(1.69) | 33.11 |
| | SR [4] | Axial Only | 14.65(0.52) | 14.72 | 0.30(0.05) | 0.30 | 0.15(0.01) | 0.16 | 32.58(2.58) | 32.48 |
| | 3D-SRU-Net [5] | Axial and Sagittal | 19.07(0.69) | 19.17 | 0.61(0.05) | 0.62 | 0.19(0.01) | 0.20 | 15.16(0.33) | 15.15 |
| | 3D-Y-Net-GAN | Axial and Sagittal | 19.65(0.81) | 19.58 | 0.68(0.04) | 0.69 | **0.21(0.01)** | **0.21** | 14.16(1.77) | 13.65 |
| | Ours Full | Axial and Sagittal | **19.75(0.85)** | **19.69** | **0.69(0.05)** | **0.71** | **0.21(0.02)** | **0.21** | **13.90(1.79)** | **13.40** |
| Independent Testing Dataset 1 | Bicubic [13] | Axial Only | 13.59(0.92) | 13.74 | 0.27(0.06) | 0.28 | 0.16(0.01) | 0.16 | 35.32(3.88) | 34.25 |
| | SR [4] | Axial Only | 13.83(0.95) | 13.96 | 0.28(0.06) | 0.29 | 0.15(0.01) | 0.15 | 35.26(3.87) | 34.13 |
| | 3D-SRU-Net [5] | Axial and Sagittal | 17.63(1.27) | 17.47 | 0.57(0.06) | 0.57 | 0.17(0.02) | 0.17 | 18.29(2.77) | 18.34 |
| | 3D-Y-Net-GAN | Axial and Sagittal | 18.00(1.41) | 17.63 | 0.60(0.07) | 0.60 | 0.18(0.02) | 0.18 | 17.00(2.96) | 17.15 |
| | Ours Full | Axial and Sagittal | **18.18(1.44)** | **17.86** | **0.61(0.08)** | **0.61** | **0.19(0.02)** | **0.19** | **16.93(2.95)** | **16.98** |
| Independent Testing Dataset 2 | Bicubic [13] | Axial Only | 13.76(1.20) | 14.26 | 0.27(0.07) | 0.28 | 0.16(0.01) | 0.16 | 34.16(4.95) | 32.03 |
| | SR [4] | Axial Only | 13.66(1.03) | 14.04 | 0.23(0.05) | 0.23 | 0.14(0.01) | 0.14 | 35.33(4.33) | 33.18 |
| | 3D-SRU-Net [5] | Axial and Sagittal | 18.14(1.55) | 18.84 | 0.56(0.08) | 0.58 | 0.19(0.02) | 0.19 | 17.25(3.27) | 15.95 |
| | 3D-Y-Net-GAN | Axial and Sagittal | 18.41(1.71) | 19.01 | 0.59(0.09) | 0.62 | 0.19(0.02) | **0.20** | **16.32(3.48)** | 15.13 |
| | Ours Full | Axial and Sagittal | **18.56(1.72)** | **19.17** | **0.61(0.09)** | **0.64** | **0.20(0.03)** | **0.20** | 16.40(3.47) | **15.07** |

Bold text indicates the best performance. We show an extra metric mean absolute error (MAE) for quantitative evaluation of residual images. Note that all the metrics are calculated based on 8-bit grayscale images.

$\mathbf{I}^S$ and $\mathbf{I}^{GT}$. The mini-batch size and epoch are set to 16 and 200, respectively. For the generator, we use the Adam optimizer [29] with the momentum parameter $\beta_1$=0.9 and adopt a stepwise, exponential-decay learning rate schedule with initial value=5×10$^{-4}$, decay step=252, and decay rate=0.989. We use the same optimizer and learning rate schedule for the discriminator. We initialize the generator and the discriminator with an He normal initializer [30]. We set $\lambda_1$, $\lambda_2$, and $\lambda_3$ in $L_G$ to be 0.2, 0.02, and 0.1, respectively.

For 3D-DenseU-Net, we randomly sample 80 patches per volume with a size of 48×48×48. The mini-batch size and epoch are set to 12 and 300, respectively. We use the Adam optimizer with $\beta_1$=0.9 and adopt a stepwise, exponential-decay learning rate schedule with initial value=5×10$^{-4}$, decay step=373, and decay rate=0.989. We initialize it with the He normal initializer and set $\lambda_1$and $\lambda_3$ in its loss function to 1 and 0.001, respectively. Note that not like training, inference is not patch-based. On the contrary, it is based on whole MR images. Therefore, no special post-processing is needed in our method.

For the SR [4] method, we set appropriate parameters for coupled dictionary training. Concretely, we set dictionary size=512, patch number=100,000, patch size=13×13, sparsity regularization=0.15, and overlap=12. Notably, for bicubic interpolation and SR methods, we only utilize axial thick-section MR images given their limitations.

For 3D-SRU-Net, we choose appropriate hyper-parameters to guarantee its best performance while maintaining good comparability. Concretely, we consider the patch size of 32×32×15 for $\mathbf{I}^A$ and 32×32×120 for $\mathbf{I}^S$ and $\mathbf{I}^{GT}$. We set the mini-batch size and epoch to 32 and 300, respectively. We adopt the Adam optimizer with a parameter of $\beta_1$ =0.9, initial learning rate=5×10$^{-4}$, and the bicubic-weighted MSE loss function as adopted in [5].

The SR method was implemented in MATLAB2017a. The training process took approximately 10 hours, while the reconstruction process took approximately 2 hours per sample. All the DL methods were implemented with Python3.6.2 and TensorFlow1.3, running on a NVIDIA Titan Xp GPU with 12 GB of RAM. Our 3D-Y-Net-GAN took approximately 20 hours for training, 3D-DenseU-Net took approximately 20 hours for training, and 3D-SRU-Net took approximately 11 hours for training.

### C. ABLATION EXPERIMENT ON INPUT DATA

In this section, we design an experiment on the three aforementioned cases to demonstrate the impact of different input data. The reconstruction results of the three cases are visualized in Fig. 6. We can see that reconstructed thin-section MR images based on images in the axial and sagittal planes have more structural details and less distortion compared to images generated from single-plane thick-section images. This is because multiplanar thick-section MR images could be fused and thus contribute collaboratively to the reconstruction task. Their quantitative evaluation is summarized in Table II, which shows that the reconstruction method with multiplanar MR image fusion can generate thin-section images of higher similarity with ground-truth images.

### D. ABLATION EXPERIMENT ON LOSS FUNCTION

In this section, to validate the contribution of each term in our proposed comprehensive loss function, we set three comparison experiments to show the effectiveness of self-adaptive Charbonnier loss, gradient correction loss, and adversarial loss. Note that this ablation experiment is based on our proposed 3D-Y-Net-GAN, and we do not conduct 5-fold cross-validation here. Their reconstruction results are shown as Fig. 7. From the visualization comparison, we can see that the $\ell_1$ norm generates blurry images compared to self-adaptive Charbonnier loss. The results based on a loss function without gradient correction loss show less sharp edges compared to our proposed loss function. A loss function without adversarial loss generates less realistic images than our proposed loss function. The quantitative



2169-3536 (c) 2019 IEEE. Translations and content mining are permitted for academic research only. Personal use is also permitted, but republication/redistribution requires IEEE permission. See http://www.ieee.org/publications_standards/publications/rights/index.html for more information.

This article has been accepted for publication in a future issue of this journal, but has not been fully edited. Content may change prior to final publication. Citation information: DOI 10.1109/ACCESS.2019.2918926, IEEE Access



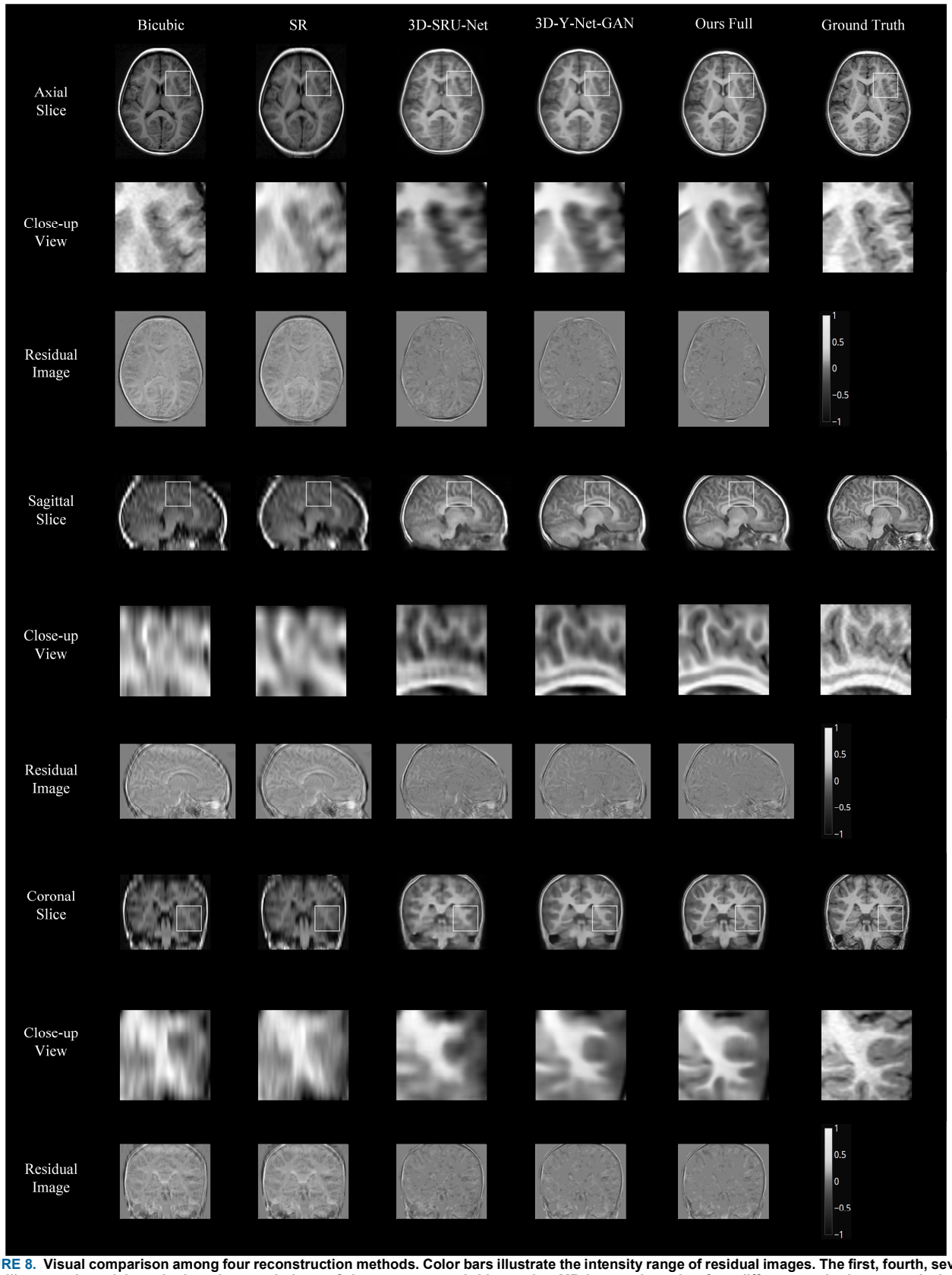


**FIGURE 8.** Visual comparison among four reconstruction methods. Color bars illustrate the intensity range of residual images. The first, fourth, seventh rows illustrate the axial, sagittal, and coronal views of the reconstructed thin-section MR images by using four different methods, respectively. The second, fifth, and eighth rows illustrate the local enlarged views. The third, sixth, and ninth rows illustrate the error maps.



2169-3536 (c) 2019 IEEE. Translations and content mining are permitted for academic research only. Personal use is also permitted, but republication/redistribution requires IEEE permission. See http://www.ieee.org/publications_standards/publications/rights/index.html for more information.

This article has been accepted for publication in a future issue of this journal, but has not been fully edited. Content may change prior to final publication. Citation information: DOI 10.1109/ACCESS.2019.2918926, IEEE Access



evaluation shown in Table III further validates the contribution of our proposed loss function.

### E. COMPARISON WITH OTHER METHODS

In this section, we design a comparison experiment to evaluate our proposed method by comparing it with three existing methods, traditional bicubic interpolation [13], sparse representation [4], and 3D-SRU-Net [5]. In addition, we also illustrated the result of the first-stage 3D-Y-Net-GAN, to validate the effectiveness of the second-stage network. The reconstruction results of a certain slice in the center of the sampling intervals are visualized in Fig. 8. Compared to the other three methods, our proposed reconstruction framework generates the most realistic MR images, which is closer to the ground truth on the rightmost column of Fig. 8.

The traditional bicubic interpolation method shows blurry reconstructed results and suffers from severe detail distortion as well as artifacts, partly due to its limited receptive fields, untrainable structure, and lack of sagittal information.

The sparse representation method generates smoother results with relatively better tissue coherency than bicubic interpolation but still outputs poor results in the sagittal and coronal planes for its 2-D receptive field and limited modeling capacity.

While 3D-SRU-Net reconstructed thin-section MR images with less artifacts, it provided worse results than our proposed framework. Two factors can account for its worse performance. First, given its single-stage architecture, 3D-SRU-Net suffers from inevitable insufficiency in modeling capacity and thus cannot provide a balance among feature fusion, upsampling, and detail preservation, which leads to a poor performance in the sagittal plane reconstruction. Second, an upscaling *Path 1-8* based on shallow features passes through the top-level skip connection. Potential downsides of this design are that features with severe artifacts caused by fractionally-strided convolution with a small kernel size and a very large upscaling factor is directly passed to last several layers through the top-level connection, which harms the reconstruction results.

In the close-up views, we note that our framework reconstructs realistic images that are spatially closer to the ground truth after the first-stage reconstruction and recovers more tissue details in sagittal and coronal planes after the detail recalibration of the second stage, which reflects the effectiveness of our proposed two-stage reconstruction framework.

The overall experimental results are summarized in Table IV, in which we compare the mean values, standard deviations, and median values of the above metrics. We show the experimental results on three different datasets to illustrate the generalizability and robustness of our proposed method.

Our method outperforms existing methods on all three datasets, with higher PSNR, SSIM, NMI, and mean absolute error (MAE). Specifically, in contrast to the untrainable bicubic interpolation method, our method can learn from training samples to generate images with better tissue coherency. Compared to the SR method, our method can utilize 3-D receptive fields and greater modeling capacity to recover more realistic thin-section images. Also, notice that SR method has worse statistical results on the independent testing dataset 2 than on independent testing dataset 1, which shows that our model has better robustness than SR method when dealing with different datasets. Compared to 3D-SRU-Net, our full framework can better learn mapping from the thick-section MR images to corresponding thin-section MR images, which means dealing with feature fusion, upsampling, and detail recalibration separately and successively will assign a clear task to the neural networks given their limited modeling capacity. This improvement in the final results further confirms the superiority of our proposed method. Note that our model not only shows better performance on cross-validation dataset, but also shows better reconstruction quality on two more testing datasets. Also, since the number of testing data samples in our experiments is around 4 times as many as the training data samples we used, our proposed reconstruction framework shows good generalizability and robustness to be applied to larger database.

## IV. CONCLUSION

We proposed a two-stage reconstruction framework to reconstruct thin-section infant head MR images from thick-section images in the axial and sagittal planes. Our proposed 3D-Y-Net-GAN, trained on paired patches of thick-section MR images, reconstructed preliminary thin-section MR images for subsequent refinement. Then, based on the output of the first stage and original thick-section images, our proposed 3D-DenseU-Net was trained for further detail refinement and performance improvement. Moreover, we proposed a comprehensive loss function composed of a self-adaptive Charbonnier loss, a 3-D gradient correction loss, an adversarial loss, and an $\ell_2$ weight regularization loss for more effective and more realistic reconstruction.

Two ablation experiments on different input data and our proposed loss function have been conducted. The visualization and quantitative evaluation demonstrated that our proposed multiplanar image fusion and comprehensive loss function could contribute to performance improvement in reconstruction. A comparison experiment with three existing methods was conducted based on a cross-validation dataset and two independent testing datasets. The quantitative evaluation revealed that our proposed method is able to reconstruct thin-section MR images with higher PSNR, SSIM, and NMI compared to the other three methods, including traditional bicubic interpolation [13], sparse representation [4], and 3D-SRU-Net [5]. Note that we show mean absolute error to demonstrate that our reconstruction results have lower residues by average, where we use 8-bit grayscale for evaluation. Even though MAE of Ours Full is a little bit worse than that of our first stage network on independent testing dataset 2, our full model still shows overall better reconstruction details because its loss function



2169-3536 (c) 2019 IEEE. Translations and content mining are permitted for academic research only. Personal use is also permitted, but republication/redistribution requires IEEE permission. See http://www.ieee.org/publications_standards/publications/rights/index.html for more information.

This article has been accepted for publication in a future issue of this journal, but has not been fully edited. Content may change prior to final publication. Citation information: DOI 10.1109/ACCESS.2019.2918926, IEEE Access



focuses on penalizing outlier pixel predictions to generate more realistic images. In addition, we illustrated visualized results generated from the above four methods to bolster the superiority of our method's performance compared to other methods. Although the objective of our proposed method is the reconstruction of thin-section infant head MR images from thick-section images in axial and sagittal planes, it can be easily extended to other application contexts, such as three-plane reconstruction or adult head MR image reconstruction. Furthermore, this reconstruction method can also be used to normalize image layer spacing, to benefit data-driven researches based on image big data.

Data preprocessing is an important factor to guarantee the applicability of our proposed reconstruction framework. We apply unified spatial normalization, histogram matching, and grayscale normalization to all MR images to mitigate the impacts caused by their various intensities and contrast ranges. We also adopt data augmentation to enlarge our training dataset. In future work, we will generalize our reconstruction method and perform validation on more data of different categories.

## ACKNOWLEDGMENT

This work was supported by the National Natural Science Foundation of China (61471125), the National Basic Research Program of China (2015CB755500), and Shanghai Shenkang Hospital Development Center Clinical Auxiliary Capacity (Imaging Medicine) Construction Project (SHDC22015031).

## REFERENCES

[1] A. P. Mahmoudzadeh, N. H. Kashou, "Interpolation-based super-resolution reconstruction: effects of slice thickness," *J. Med. Imag.*, vol. 1, no. 3, pp. 034007, Dec. 2014.

[2] A. P. Mahmoudzadeh, N. H. Kashou, "Evaluation of Interpolation Effects on Upsampling and Accuracy of Cost Functions-Based Optimized Automatic Image Registration," *Int. J. Biomed. Imag.,* vol. 2, no. 395915, pp. 31-39, Aug. 2013.

[3] Q. Lin, Q. Zhang and L. Tongbin, "Slice Interpolation in MRI Using a Decomposition-Reconstruction Method," in *Proc. ICISCE*, Changsha, China, 2017, pp. 678-681.

[4] J. Yang, J. Wright, T. Huang, and Y. Ma, "Image super-resolution via sparse representation," *IEEE. Trans. Image Process.*, vol. 19, no. 11, pp. 2861–2873, Nov. 2010.

[5] L. Heinrich, J. A. Bogovic, S. Saalfeld, "Deep learning for Isotropic Super-resolution from Non-isotropic 3D Electron Microscopy," in *Proc. MICCAI*, Quebec City, Canada, 2017, pp. 135-143.

[6] Z. Li, Y. Wang, J. Yu, "Reconstruction of Thin-Slice Medical Images Using Generative Adversarial Network," in *Proc. MICCAI*, Quebec City, Canada, 2017, pp. 325-333.

[7] S. McDonagh *et al.*, "Context-Sensitive Super-Resolution for Fast Fetal Magnetic Resonance Imaging," in *Proc. MICCAI RAMBO*, Quebec City, Canada, 2017, pp. 116-126.

[8] M. Mardani, E. Gong, J. Y. Cheng, S. Vasanawala, G. Zaharchuk, M. T. Alley, N. Thakur, S. Han, W. J. Dally, J. M. Pauly, and L. Xing, "Deep generative adversarial networks for compressed sensing automates MRI," *IEEE Trans. Med. Imag.*, to be published.

[9] O. Ronneberger, P. Fischer, T. Brox, "U-Net: Convolutional Networks for Biomedical Image Segmentation," in *Proc. MICCAI*, Munich, Germany, 2015, pp. 234-241.

[10] C. Ledig, L. Theis, F. Huszar, J. Caballero, A. Cunningham, A. Acosta, *et al.*, "Photo-realistic single image super-resolution using a generative adversarial network," in *Proc. CVPR*, Honolulu, HI, USA, 2017, pp. 105-114.

[11] B. Lim, S. Son, H. Kim, S. Nah, K. M. Lee, "Enhanced Deep Residual Networks for Single Image Super-Resolution," in *Proc. CVPR*, Honolulu, HI, USA, 2017, pp. 1132-1140.

[12] X. Mao, Q. Li, H. Xie, R. Y.K. Lau, Z. Wang, and S. P. Smolley, "Least-squares generative adversarial networks," in *Proc. ICCV*, Venice, Italy, 2017, pp. 2813-2821.

[13] R. Keys, "Cubic convolution interpolation for digital image processing," in *IEEE Trans. Acoust., Speech, Signal Processing*, vol. 29, no. 6, pp. 1153-1160, Dec. 1981.

[14] M. D. Zeiler, G. W. Taylor and R. Fergus, "Adaptive deconvolutional networks for mid and high level feature learning," 2011 International Conference on Computer Vision, Barcelona, 2011, pp. 2018-2025.

[15] W. Shi, J. Caballero, F. Huszar *et al.*, "Real-Time Single Image and Video Super-Resolution Using an Efficient Sub-Pixel Convolutional Neural Network," in *Proc. CVPR*, Las Vegas, NV, USA, 2016, pp.1874-1883.

[16] C. Dong, C. Loy Chen, K. He, X. Tang, "Image Super-Resolution Using Deep Convolutional Networks," *IEEE Trans. Pattern Anal. Machine Intell.*, vol. 38, no. 2, pp. 295-307, Feb. 2016.

[17] J. Kim, J. K. Lee, K. M. Lee, "Accurate Image Super-Resolution Using Very Deep Convolutional Networks," in *Proc. CVPR*, Las Vegas, NV, USA, 2016, pp. 1646-1654.

[18] S. Zhang, G. Liang, S. Pan and L. Zheng, "A Fast Medical Image Super Resolution Method Based on Deep Learning Network," in *IEEE Access*, vol. 7, pp. 12319-12327, 2019.

[19] H. Lu, Y. Li, S. Nakashima, H. Kim and S. Serikawa, "Underwater Image Super-Resolution by Descattering and Fusion," in *IEEE Access*, vol. 5, pp. 670-679, 2017.

[20] W. Lai, J. Huang, N. Ahuja, M. Yang, "Deep Laplacian Pyramid Networks for Fast and Accurate Super-Resolution," in *Proc. CVPR*, Honolulu, HI, USA, 2017, pp. 5835-5843.

[21] Y. Zhang, Y. Tian, Y. Kong, B. Zhong, Y. Fu, "Residual Dense Network for Image Super-Resolution," *arXiv preprint* arXiv: 1802.08797.

[22] P. Ramachandran, B. Zoph, Q. V. Le, "Searching for Activation Functions," *arXiv preprint* arXiv: 1710.05941.

[23] M. Mirza, S. Osindero, "Conditional Generative Adversarial Nets," *arXiv preprint* arXiv: 1411.1784.

[24] G. Qi, "Loss-Sensitive Generative Adversarial Networks on Lipschitz Densities," *arXiv preprint* arXiv: 1701.06264.

[25] G. Huang, Z. Liu, L. Maaten, K. Q. Weinberger, "Densely Connected Convolutional Networks," in *Proc. CVPR*, Honolulu, HI, USA, 2017, pp. 2261-2269.

[26] D. Chard, G. Parker, C. Griffin, A. Thompson, D. Miller, "The reproducibility and sensitivity of brain tissue volume measurements derived from an SPM-based segmentation methodology," *J. Magn. Reson. Imag.*, vol. 15, no. 3, pp. 259-267, Mar. 2002.

[27] F. Shi, P. Yap, G. Wu, H. Jia, J. H. Gilmore, W. Lin, D. Shen, "Infant Brain Atlases from Neonates 1- and 2-Year-Olds," *Plos One*, vol. 6, no. 4, pp. e18746, Apr. 2011.

[28] H. Salehinejad, S. Valaee, T. Dowdell, and J. Barfett, "Image Augmentation using Radial Transform for Training Deep Neural Networks," *arXiv preprint* arXiv: 1708.04347v4.

[29] D. Kingma, and J. Ba, "Adam: A Method for Stochastic Optimization," in *Proc. ICLR*, Vancouver, Canada, 2015, pp. 1-13.

[30] K. He, X. Zhang, S. Ren, and J. Sun, "Delving Deep into Rectifiers: Surpassing Human-Level Performance on ImageNet Classification," in *Proc. ICCV*, 2015, Santiago, Chile, pp.1026-1034.



2169-3536 (c) 2019 IEEE. Translations and content mining are permitted for academic research only. Personal use is also permitted, but republication/redistribution requires IEEE permission. See http://www.ieee.org/publications_standards/publications/rights/index.html for more information.

This article has been accepted for publication in a future issue of this journal, but has not been fully edited. Content may change prior to final publication. Citation information: DOI 10.1109/ACCESS.2019.2918926, IEEE Access

**JIAQI GU** received the B.Sc. degree in microelectronic science and engineering from Fudan University, Shanghai, China in 2018. He is currently a post-graduate student studying for his Ph.D. degree in the Department of Electrical and Computer Engineering, The University of Texas at Austin. His current research interests include medical image processing and machine-learning application.

**ZHONGWEI QIAO** received the M.D. degree from Shanghai Jiao Tong University, Shanghai, China. He was a Postdoctoral Fellow at Hong Kong University. He is currently Chief Radiologist and Director at Department of Radiology of Children's Hospital, Fudan University, and Principle Investigator in Pediatrics at Institute of Functional and Molecular Medical Imaging, Fudan University. His research intresets include Pediatric Radiology and AI in Radiologic Diagnosis.

**ZEJU LI** received the B.Sc. and M.S. degree in eletronic engineering from Fudan University, China in 2018. He is currently a post-graduate student studying for his Ph.D. degree in the Department of Computing, Imperial College London. His current research interests include biomedical image processing and deep-learning application.

**JINHUA YU** received the Ph.D. degree in electronic engineering from Fudan University, Shanghai, China, in 2008.
From 2008 to 2010, she was a Postdoctoral Fellow with the Department of Bioengineering, University of Missouri, Columbia, MO.
She is currently a Full Professor in Electronic Engineering Department of Fudan University. Her current research interests include medical signal analysis, radiomics, and ultrasound imaging.

**YUANYUAN WANG** received the B.Sc., M.Sc. and Ph.D. degrees in electronic engineering from Fudan University, Shanghai, China, in 1990, 1992 and 1994, respectively.
During 1994 to 1996, he was a Postdoctoral research Fellow with the School of Electronic Engineering and Computer Science at University of Wales, Bangor, UK. In May 1996, he went back to Department of Electronic Engineering at Fudan University as an associate professor. He was then promoted to a full professor in May, 1998. He is currently the director of Biomedical Engineering Center at Fudan University. He is also the author or coauthor of 6 books and 500 research papers. His research interests include medical ultrasound techniques and medical image processing.

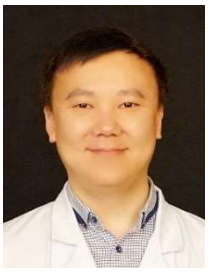

**HAOWEI YANG** received the Master of Medicine Degree in Fudan University, Shanghai, China, in 2011. From 2009 to present, he was a attending doctor in Radiology Department of Children's Hospital of Fudan University. During the period of postgraduate study, he research on DTI analysis of temporal lobe epilepsy, and continue with further study of imaging epilepsy.



2169-3536 (c) 2019 IEEE. Translations and content mining are permitted for academic research only. Personal use is also permitted, but republication/redistribution requires IEEE permission. See http://www.ieee.org/publications_standards/publications/rights/index.html for more information.